Field-induced polarization rotation and phase transitions in 0.70Pb(Mg_{1/3}Nb_{2/3})O_{3}-0.30PbTiO_{3} piezoceramics observed by in situ high-energy x-ray scattering

Dong Hou, Tedi-Marie Usher, Lovro Fulanovic, Marko Vrabelj, Mojca Otonicar, Hana Ursic, Barbara Malic, Igor Levin, and Jacob L. Jones

Phys. Rev. B **97**, 214102 — Published 12 June 2018

DOI: 10.1103/PhysRevB.97.214102

Field-induced polarization rotation and phase transitions in $0.70Pb(Mg_{1/3}Nb_{2/3})O_3$-$0.30PbTiO_3$ piezoceramic observed by *in situ* high-energy X-ray scattering

Dong Hou[1], Tedi-Marie Usher[1, 2], Lovro Fulanovic[3], Marko Vrabelj[3], Mojca Otonicar[3], Hana Ursic[3], Barbara Malic[3], Igor Levin[4], and Jacob L. Jones[1, a]

[1] Department of Materials Science and Engineering, North Carolina State University, Raleigh, NC 27695, USA

[2] Neutron Scattering Division, Oak Ridge National Laboratory, Oak Ridge, TN 37831, USA

[3] Electronic Ceramics Department, Jožef Stefan Institute, 1000 Ljubljana, Slovenia

[4] Materials Measurement Science Division, National Institute of Standards and Technology, Gaithersburg, MD 20899, USA

Abstract

Changes to the crystal structure of $0.70Pb(Mg_{1/3}Nb_{2/3})O_3$-$0.30PbTiO_3$ (PMN-0.30PT) piezoceramic under application of electric fields at the long-range and local scale are revealed by *in situ* high-energy X-ray diffraction (XRD) and pair distribution function (PDF) analyses, respectively. The crystal structure of unpoled samples is identified as monoclinic *Cm* at both the long-range and local scale. *In situ* XRD results suggest that field-induced polarization rotation and phase transitions occur at specific field strengths. A polarization rotation pathway is proposed based on the Bragg peak behaviors and the Le Bail fitting results of the *in situ* XRD patterns. The PDF results show systematic changes to the structures at the local scale, which is in agreement with the changes inferred from the *in situ* XRD study. More importantly, our results prove that polarization rotation can be detected and determined in a polycrystalline relaxor ferroelectric. This study supports the idea that multiple contributions, specifically ferroelectric-ferroelectric phase transition and polarization rotation, are responsible for the high piezoelectric properties at the morphotropic phase boundary of PMN-*x*PT piezoceramics.

a Author to whom correspondence should be addressed. Electronic mail: jacobjones@ncsu.edu

1 Introduction

$Pb(Mg_{1/3}Nb_{2/3})O_3$ (PMN) with the perovskite ABO_3 structure is the best known canonical relaxor, which shows unusually large dielectric constant in a wide temperature range with a characteristic strong frequency-dependence.[1–3] Alloying of the classical ferroelectric $PbTiO_3$ (PT) with PMN results in the solid solution $(1-x)Pb(Mg_{1/3}Nb_{2/3})O_3$-$xPbTiO_3$ (or PMN-*x*PT), which is one of the most extensively studied relaxor ferroelectric systems.[4–7] Morphotropic phase boundary (MPB) regions were reported in PMN-*x*PT, separating different phases on the low-PT and high-PT sides, i.e., rhombohedral/monoclinic phases at x~0.30–0.31, and monoclinic/tetragonal phases at x~0.35–0.37, respectively.[8–10] Giant piezoelectric responses, e.g. high piezoelectric coefficients, extremely large strains, and high electromechanical coupling factors have been reported in compositions near the MPB.[5,7,11,12] Therefore, PMN-*x*PT and other relaxor-based systems have received considerable attention from academia and industry, and have been integrated into numerous applications and devices, such as new generation electromechanical sensors, actuators, and transducers.[5,6,12]

PMN-*x*PT has high degree of structural complexity, e.g. highly complex microstructures, long-range crystallographic structures, and cation order/disorder at the local scale.[6,13,14] Debate exists on the most accurate description of the structures at different length scales. A full understanding of the microscopic origin of the excellent piezoelectric properties is still in development. In general, both intrinsic and extrinsic effects contribute to the dielectric and piezoelectric responses.[12,15,16] The extrinsic contribution comes from the presence or displacement of defects and domain walls. The intrinsic effects are related to the changes of the lattice itself, such as lattice distortion, symmetry changes, etc.[12] Some corresponding mechanisms related to the two contributions in PMN-*x*PT *single crystals* have been reported

based on experimental and theoretical studies, such as electric-field-induced phase transitions, polarization rotation in monoclinic phases, adaptive domain structures, existence of polar nano-regions (PNRs), and so on.[17–21] These theories have co-existed in the community for decades, and a detailed review can be found in Davis.[22] Since the discovery of high piezoelectricity in PMN-*x*PT, intensive fundamental studies have focused on single crystals but not on ceramics. The major problem in preparing PMN-*x*PT ceramics has been the formation of secondary pyrochlore phase, inhibiting the dielectric and piezoelectric properties.[23] This "secondary phase problem" has been solved (or significantly alleviated) by carefully engineering and improving the synthesis procedures.[23–25] Compared to the time consuming, costly, and shape/size-restricted single crystals, PMN-*x*PT piezoceramics can be a suitable replacement in many applications.

Among the limited fundamental studies on PMN-*x*PT piezoceramics, the major mechanism for the anomalous piezoelectric response near the MPB was proposed to be extrinsic, arising from enhanced domain switching. But based on studies of a variety of perovskite piezoceramics, (e.g. PZT,[26] potassium sodium niobate,[27] sodium bismuth titanate,[28] and barium titanate[29]), other effects, such as field-induced phase transitions, the existence of lower symmetry phase(s), and/or polarization rotation, may play crucial roles also. Only most recently, the intrinsic contribution of PMN-0.325PT ceramics have been studied by Liu *et al.* and an electric-field-driven continuous polarization rotation in monoclinic phases was proposed as the mechanism.[30,31] However, considering the high complexity of PMN-*x*PT piezoceramics, direct evidence of the intrinsic electric-field-induced effects at both the long-range and local scale are not yet available. Therefore, in order to clarify the origin of ultrahigh piezoelectricity in PMN-*x*PT piezoceramics near the MPB, a comprehensive investigation of the structure under the application of electric fields is presented. The composition chosen in this study is PMN-0.30PT,

which is located on the low-PT side of the MPB based on the most recent phase diagram.[8] Here, a mechanochemical synthesis procedure is used to ensure chemical homogeneity of the sample.[24] Moreover, the sintering process is purposefully designed to optimize the grain size of the samples to be around 1 μm for scattering measurements. The field-induced structural changes are investigated using *in situ* XRD and PDF at a synchrotron source. The long-range (from XRD) and local (from PDF) structural changes during the application of electric fields can be monitored and determined.[32,33] Our results evidence multiple effects in PMN-0.30PT, including polarization rotation and ferroelectric-ferroelectric phase transitions, elucidating the origins of the enhanced piezoelectric properties of the PMN-*x*PT piezoceramics near the MPB.

2 Experimental

PbO (99.9%, Aldrich[1]), MgO (98%, Aldrich), TiO_2 (99.8%, Alfa Aesar) and Nb_2O_5 (99.9%, Aldrich) were used to synthesize the stoichiometric PMN-0.30PT powders. The homogenized powder mixture was high-energy milled in a planetary ball mill (model: Retsch PM 400) at 300 rpm for up to 48 hours, and additionally in an attrition mill (model: Netzsch PE075/PR01) at 800 rpm for 4 hours in isopropanol. The powder compacts were pressed uniaxially at 50 MPa, then isostatically at 300 MPa, and sintered in double alumina crucibles in the presence of packing powder at 1200 °C for 2 hours, with heating and cooling rate of 5 °C/min.

The microstructure was characterized with a field-emission scanning electron microscope (FE-SEM; model: JEOL JSM-7600). The samples were polished, thermally etched at 900 °C, and coated by a sputter coater (model: BAL-TEC SCD 005) prior to the FE-SEM imaging. The

[1] Any mention of commercial products is for information only; it does not imply recommendation or endorsement by NIST.

grain size was determined from a stereological analysis of the FE-SEM micrographs, for which more than 300 grains per sample were measured. Transmission electron microscopy (TEM) was performed in a Philips CM30 operated at 200 kV. The samples for TEM were prepared using mechanical polishing, followed by ion-thinning (4.0 kV, T=-100 °C) until perforation.

For the electrical measurements, the pellets were cut to a thickness of about 200 μm, polished, and annealed at 600 °C for 1 hour. The Cr/Au electrodes were deposited using RF-magnetron sputtering (5 Pascal). The polarization-electric-field (P-E) hysteresis loops were measured with an analyzer (model: aixACCT Analyzer TF 2000) at 1 Hz using a sinusoidal waveform. The dielectric permittivity ε' and the dielectric losses $\tan\delta$ as a function of temperature and frequency were measured with a LCR impedance meter (model: HP4192A) in the temperature range of 30-300 °C. The dielectric data were collected during cooling using a step of 1 °C.

For the long-range structural studies, *in situ* high-energy synchrotron XRD (SXRD) measurements were carried out at the beamline 11-ID-B of the Advanced Photon Source at Argonne National Laboratory.[34,35] The pellets were cut into ceramic bars with an approximate size of 1.0×1.0×5.0 mm^3, annealed to relieve stress introduced by cutting, and silver electrodes were deposited on two 1.0×5.0 mm^2 opposing faces. The design of the electric field loading stage is the same as described by Usher *et al.*[36] The samples were measured in transmission mode using a slit size of 0.5×0.5 mm^2 and a wavelength of 0.21140 Å (58.64910 keV). A 99% absorption is calculated for a depth of 5.2 mm using Beer's law, whereas the sample thickness is only 1 mm in the direction of the beam. Thus, we consider this configuration to be an ideal balance between large grain averaging (larger thickness is preferred) and high transmission (smaller thickness is preferred). The samples were immersed in the dielectric insulating liquid

Fluorinert™ FC-40 to mitigate electrical breakdown. The XRD patterns were collected before and during the application of static electric fields to unpoled samples. The collecting time is five minutes at each field step using a Perkin Elmer detector with a sample-detector distance of 0.70 m. The vertical sector of the 2-D XRD image, which measures scattering vectors approximately *parallel* to the electric field direction, was reduced to a 1-D pattern by integrating an azimuthal 20° sector in the FIT2D software.[37] Full-profile analyses of the 1-D patterns were performed using the software package General Structural Analysis Software (GSAS)[38] with the EXPGUI interface[39].

In situ total scattering measurements were conducted in order to study the local structure. The setup is similar to the XRD measurements as described above, but the detector was moved much closer to the sample, with a sample-detector distance of 0.18 m, to ensure that a sufficiently high scattering vector (Q) can be obtained for the PDF analysis. 1-D patterns were integrated from the vertical sector of the 2-D scattering images using FIT2D.[37] The reduced datasets were corrected for polarization, and then normalized and converted to total scattering function $S(Q)$. The PDF $G(r)$ pattern was converted from $S(Q)$ using a conventional formalism involving the sine Fourier transform in PDFgetX3 program.[40] The PDF calculation is described as:

$$G(r) = \frac{2}{\pi}\int_0^\infty Q(S(Q)-1)\sin(Qr)\,dQ \qquad (1)$$

where r is the atom-atom correlation distances. Note that the directional $S(Q)$ is reduced from the *parallel* to electric field section of the 2-D scattering image, therefore, the Fourier transformed $G(r)$ only incorporates contributions from crystallites having their Q_{hkl} vectors approximately *parallel* to the electric field direction. Background scattering from air and insulating liquid was subtracted during data processing. Real-space least-squares refinements to the PDFs were carried

out using PDFgui.[41] PDF peak fitting was conducted using a Gaussian profile. In addition, cerium dioxide standard was used for *in situ* XRD and PDF to calibrate the sample to detector distance, beam center, and detector orthogonality.

3 Results and Discussions

3.1 Micrographs, polarization, and permittivity of PMN-0.30PT piezoceramic

The FE-SEM images of the etched surfaces are shown in Fig. 1a, indicating homogeneous and uniform microstructures of the synthesized samples. The relative density (RD) is 96.3 $\pm$ 0.1% of theoretical density (8.17 g cm^{-3} according to the JCPDS database [reference code 01-081-0861]). Grain size is found to be 1.1 $\pm$ 0.6 μm according to the stereological analysis, which is ideal for XRD and total scattering measurements. Figure 1b shows the relative dielectric permittivity as a function of temperature at 1, 10, and 100 kHz frequencies. The permittivity reaches a maximum of $\varepsilon'_{max}\approx$39200 at 140 °C at 1 kHz, while at room temperature $\varepsilon'\approx$3400. These values are relatively high compared to other dielectric ceramics, and are even comparable with single crystals.[24,42,43] The permittivity peak is broad with a full width at half maximum (FWHM) around 50 °C, and is frequency dispersive. A strong deviation to the Curie-Weiss law (T_{dev}) occurs at 242 °C, which is around 100 °C above T_m. In addition, the dielectric loss ($\tan\delta$ in Fig. 1b) also shows a frequency dependence. The dielectric behaviors suggest a relaxor character of the PMN-0.30PT piezoceramic. The P-E hysteresis loops are shown in Fig. 1c. The P-E loop saturates at 4.0 kV/mm, with a remnant polarization (P_r) of 30 μC/cm^2 and a coercive field (E_c) of 0.87 kV/mm, revealing a ferroelectric character of the sample. Therefore, the property tests indicate that the PMN-0.30PT piezoceramic presents a combined behavior of a typical relaxor (like PMN) and a classic ferroelectric (like PT).

In order to construct a clear understanding of the structure-property relationships in PMN-0.30PT piezoceramic, the long-range and local structure of unpoled samples are presented in Sections 3.2. The field-induced structural changes at the long-range and local scale are described

and discussed in Sections 3.3 and 3.4. The reversibility of the field-induced structural changes is discussed in Section 3.5.

3.2 Structure identification of unpoled PMN-0.30PT piezoceramic

Both laboratory XRD (Cu $K_{\alpha,1}$ radiation in reflection mode) and SXRD (synchrotron X-ray diffraction in transmission mode) patterns are obtained for the same unpoled sample as shown in Fig. 2. The major Bragg peaks suggest a typical perovskite structure. Clear peak splitting and asymmetry are shown for high 2θ Bragg peaks on the laboratory XRD in the inset of Fig. 2a. The peaks from SXRD also show asymmetry, and this is demonstrated in Fig. S1 by fitting several peaks to a Pearson VII profile shape function and calculating the degree of asymmetry. The asymmetry in peaks (220), (222), and (400) can tentatively be used to exclude rhombohedral and tetragonal, indicating a lower symmetry monoclinic phase in the unpoled sample. Without further indication, reflections in this paper are noted with a pseudocubic (PC) unit cell index.

Full-profile Rietveld refinement was also conducted on both laboratory XRD and SXRD patterns for detailed structure determination of unpoled PMN-0.30PT piezoceramic. Five plausible phases are considered for the fitting procedure, including rhombohedral *R*3*m*, tetragonal *P*4*mm*, orthorhombic *Amm*2, and monoclinic *Cm* and *Pm*.[9,10,44] The results show that the monoclinic *Cm* phase yields the best agreement between the observed and calculated profiles on both patterns, the overall fits using *Cm* can be found in Fig. 2. The magnified views of representative Bragg peaks and the fits using different phases on SXRD can be found in Fig. S2. The peak shown in the first column in Fig. S2 represents the 011 reflection, which has the highest intensity, while the other 3 columns show peaks at higher Q-values ($Q = 4\pi sin(\theta)/\lambda$). It is clear the peak broadening and asymmetry at high-Q are well represented by monoclinic *Cm*.

The structural description of the *Cm* phase can be found in Table S1 and S2 in the supplementary material.

To check if there is preferred orientation in the unpoled sample, which might affect the structure determination process, the Debye-Scherrer diffraction rings from the sample were segmented into azimuthal sectors of a 10° width. The pattern within each azimuthal sector was integrated to obtain equivalent diffracted intensities as a function of Q. The pattern of the hkl-diffracted intensity within each azimuthal sector is indicative of the structural state of grains. As shown in Fig. S3, the patterns from different azimuthal sectors are essentially equivalent, suggesting the crystallites and domains are randomly oriented. Moreover, for our Rietveld refinement on the SXRD data, we integrated the entire 2-D pattern through 360° in the azimuthal direction, mitigating any possible effects from preferred orientation in the result. Therefore, texture is neither modeled nor considered prevalent in these initial unpoled sample.

Vanderbilt and Cohen predicted the existence of three types of monoclinic metastable phases (referred as M_A, M_B, and M_C) using eighth-order expansion of the Landau free energy functional.[45] Unlike tetragonal (T), rhombohedral (R), or orthorhombic (O) structures, the polarization of monoclinic phases is not fixed to a specific direction, but lies within a plane of the unit cell. Therefore, the presence of a monoclinic phase allows the polarization vector to continuously rotate in this plane – a mechanism that is generally referred to "polarization rotation." Both M_A and M_B have a *Cm* structure while M_C has a *Pm* structure. The difference between M_A and M_B is that the M_A phase has a polarization vector (P) between the R⟨111⟩ and T⟨001⟩ ($P_X=P_Y<P_Z$), whereas for the M_B phase, it is between the R⟨111⟩ and O⟨011⟩ ($P_X=P_Y>P_Z$), where z is defined as the T⟨001⟩ direction in a pseudo-cubic unit cell.[9,43] Polarization vector of the M_C phase, on the other hand, lies between O⟨011⟩ and T⟨001⟩ ($P_X\neq P_Z$

$\neq 0$, $P_Y = 0$). To determine whether the *Cm* phase of the unpoled PMN-0.30PT belongs to M_A or M_B, the polarization was calculated by the positions of the cations and anions (neglecting the contribution of electronic polarization). Based on the refined atomic coordinates, the polarization was found to be along the [0.35 0.35 1] direction, which is 26° away from the T⟨001⟩. According to the definition of M_A, the $P_x=P_y<P_z$, and the angle between [001] and the polarization is within $0° \sim 54.7°$, whereas M_B phase has $P_x=P_y>P_z$ and angle around $54.7° \sim 90°$.[30,46] Therefore, for the unpoled state, the structure was confirmed as M_A.

In addition, TEM characterization and selected area electron diffraction (SAED) were performed on the as-sintered sample, as shown in Fig. S4 in the supplementary material. The small domains with a size of 10-25 nm are revealed, consistent with the low symmetry and subtle distortions of the *Cm* phase. SAED also evidenced extensive structured diffuse scattering, which is attributed to correlated local atomic displacements. To better characterize the local structure, the PDF was obtained. Figure 3a shows the reduced total scattering function $Q[S(Q)-1]$ for the unpoled sample. Data with good signal-to-noise ratio is obtained above 20 $Å^{-1}$, suitable for PDF analysis. The resultant PDF, which can provide valuable information about local (sub-nanometer) and intermediate (few nanometers) length scales, is shown in Fig. 3b. Figure S5 compares the PDF at the local scale (2-6 Å) to a calculated PDF from a prototypical cubic perovskite model of the same composition. The asymmetric feature of the Pb-B peak and the deviation of its peak height from the model likely arise from displacements of Pb^{2+}, which is a common feature reported in Pb-based perovskites.[13,47,48] Compared to the calculated PDF, the increased peak width results from the intrinsic disorder of this material.

PDF fitting is carried out using different ranges of length scales. The fitting method utilizes a least-squares minimization to refine the PDF patterns. Lattice parameters, isotropic

atomic displacement parameters, and atom positions are refined for each phase until the best fit is obtained. Figure 3c shows the PDF refinement result using a *Cm* phase at different length scales. The fit over a range of 2-6 Å represents the local scale structure, while fit over 8-28 Å represents the intermediate scale structure. The comparison of refined PDFs from different phases can be found in Fig. S6. The results show that the crystal structure remains monoclinic *Cm* at these different length scales despite the strong B-site disorder.

By combining laboratory XRD, SXRD, TEM, and PDF, the structure for unpoled PMN-0.30PT piezoceramic is shown to be best described by the monoclinic *Cm* space group at both local and long-range scales, and corresponds to the M_A structure in Vanderbilt-Cohen notation[45].

3.3 *In situ* XRD of PMN-0.30PT piezoceramic

Figure 4a shows four representative *Q*-ranges of the *in situ* XRD patterns at sequential static electric fields. Unless noted otherwise, for all the XRD patterns, the scattering vectors are aligned with the electric fields. The first two columns are reflections of {001} and {011} family planes at low-*Q*, while the other two columns represent the peaks of {233} and {134} at high-*Q* range. In general, the peaks at low-*Q* are broad, exhibiting only subtle changes as a function of field, while structural changes can result in distinguishable differences for peaks at high-*Q*. Based on the peaks' behavior, the field-induced changes can be grouped into 3 different stages. Stage 1 is from 0 to 1.5 kV/mm, showing a continuous change of peak position as well as relative intensity. When the field increases from 1.5 kV/mm to 1.6 kV/mm, changes in the XRD pattern are noticeable in every peak across the whole diffraction pattern. Since this change occurs discontinuously, we consider 1.6 kV/mm as the starting point of Stage 2. The sudden change from 1.5 to 1.6 kV/mm cannot result from domain wall motion, in which only the relative intensity will change instead of significant peak shifting. Piezoelectric lattice strain also cannot

be responsible since piezoelectricity results in continuous changes in diffraction patterns. Additionally, in Stage 2, peaks shift right (toward higher Q, lower d-spacing) when the field increases to 2.2 kV/mm, as clearly shown in {233} and {134} peaks in Fig. 4a. Based on the above observations, the discontinuous XRD changes between 1.5 and 1.6 kV/mm are likely caused by a first-order field-induced phase transition. Further increasing the field above 2.2 kV/mm leads to peak splitting, which is apparent at high-Q but smeared out at low-Q. This XRD peak splitting indicates continuous long-range structural changes. The tested samples withstood the field to approximately 4.0 kV/mm before experiencing dielectric breakdown. Therefore, we consider 2.2-4.0 kV/mm as Stage 3 for the process.

Quantifying structural changes under fields presents a challenge because the assumption of isotropic averaging of diffracting crystallites, which underlies the Rietveld method, becomes invalid. Crystallites that are oriented differently with respect to the electric field vector will exhibit distinct lattice distortions and atomic displacements. Nevertheless, we quantify changes in the lattice distortions by assuming that the azimuthally-averaged XRD patterns under field can still be described satisfactorily using a single unit cell. Le Bail refinements are used to extract lattice parameters as a function of field.[49] This cell-constrained, whole-pattern profile fitting technique does not require knowledge of atomic positions but is sensitive to a lattice choice, which makes it possible to distinguish, for example, between the M_A and M_C-type structures.[50]

Figures S7-S10 show the representative XRD patterns and the fits at selected fields (1.5 kV/mm, 1.6 kV/mm, 2.2 kV/mm, and 4.0 kV/mm, respectively). The best fit at each field is summarized in Fig. 4b. Figure S7a shows selected Le Bail fitting of PMN-0.30PT peaks at 1.5 kV/mm, which is the end of Stage 1. A monoclinic *Cm* structure gives the best fit, as displayed in Fig. S7b. Figure 6a-c shows the lattice metrics and cell volumes of PMN-0.30PT piezoceramic

at various electric fields, extracted from the Le Bail fitting. For direct comparison between different structures, the lattice parameters of *Cm* are plotted in Fig. 5 as $a/\sqrt{2}$, $b/\sqrt{2}$, c, and β. From the unpoled state to 1.5 kV/mm, three of these parameters (*a*, *b*, and *c*) do not significantly change and the crystal structure remains as monoclinic *Cm*. Since the unpoled sample has a M_A type structure and there is no indication of a phase transition at low fields, the *Cm* structure observed in Stage 1 is conjectured to remain as M_A type, even though M_A and M_B cannot be differentiated from only the cell metrics. The monoclinic angle β shows a gradual increment under field in Stage 1, and this continuous monoclinic distortion offers an indication of the continuous polarization rotation of M_A during the application of electric fields.

When the field increases to 1.6 kV/mm, as shown in Fig. S8a, the monoclinic *Cm*-type unit cell cannot fully describe the peak profile, e.g. {114} at Q≈6.62 Å^{-1} and {134} at Q≈7.95 Å^{-1}. By comparing the data with patterns calculated from different phases, monoclinic *Pm* is assigned to the structure at 1.6 kV/mm, which belongs to M_C according to the notation from Ref. 45. In this study, the discrimination between *Pm* and *Cm* comes only from the cell metrics itself, and Le Bail fitting favors *Pm*. Therefore, the drastic jumps of the lattice parameters between 1.5 and 1.6 kV/mm, as shown in Fig. 5a-c, are attributed to a first-order M_A (*Cm*) to M_C (*Pm*) transition. A similar jump has been reported by Chen *et al.* in $BiFeO_3$ under fields, in which an M_A to M_C-like phase transition was claimed.[51] Davis *et al.* studied the electric-field-induced phase transitions in PMN-*x*PT single crystals by macroscopic strain measurements, and reported a similar M_A to M_C sequence in PMN-0.305PT and PMN-0.31PT crystals at specific temperature and field ranges.[52] When the field further increases from 1.6 kV/mm to 2.2 kV/mm, Le Bail fitting suggests *Pm* is retained, as shown in Fig. S9.

When the field is above 2.2 kV/mm, noticeable misfits between the calculated and measured XRD patterns exist in all the candidate single-phase models, especially for high-Q reflections, as shown in Fig. S10 using 4.0 kV/mm pattern as an example. The misfits indicate the inadequacy of the current single-phase models, and suggest the possible co-existence of *Pm* with another phase. Adding a tetragonal *P*4*mm* to the *Pm* phase forms a mixed-phase model, and the fits are improved. The presence of *P*4*mm* is plausible based on previous experimental observations and first principle simulations of PMN-*x*PT near the MPB.[17,53–55] The best fit of the 4.0 kV/mm pattern can be found in Fig. S10b. The changes of lattice metrics in Stage 3 are shown in Fig. 6a-c, and for the patterns fitted using the mixed-phase model, only the parameters of the *Pm* phase are plotted. As we can see, during Stage 3, the monoclinic angle β gradually increases, lattice parameter *a* increases, while lattice parameters *b, c*, and cell volume decrease, which are consistent with a continuous polarization rotation within the (010) mirror plane of the M_C structure. It is worthwhile to note that the peak splitting at Stage 3 actually results from two parts: the changes of the *Pm* structure, and the increasing fraction of the tetragonal phase due to the applied electric field. However, we only reported the transition of the monoclinic cell parameters, not the tetragonal phase fraction, because the monoclinic distortions are of interest for the polarization rotation mechanism, and can be analyzed accurately by Le Bail approach.

To summarize the *in situ* XRD study, a field-induced M_A (*Cm*) to M_C (*Pm*) phase transition and polarization rotation in the M_A and M_C phases are deduced in PMN-*x*PT piezoceramics near the MPB. The polarization rotation path and phase transformation are illustrated in Fig. 5d: with increasing field, the polarization vector rotates in the M_A $\{1\bar{1}0\}$ plane; then a $M_A \rightarrow M_C$ phase transition occurs at 1.6 kV/mm, with the polarization vector near $\langle 011 \rangle$ in the {010} plane; further increasing the field forces the polarization of some grains to rotate

within the {010} of the monoclinic M_C phase, meanwhile the tetragonal phase starts to evolve above 2.2 kV/mm in the piezoceramic. When the field is high enough, a full transition to tetragonal *P*4*mm* phase is expected. This sequence of phase transitions is also consistent with those observed in single crystals as described in Refs. 52,55.

3.4 *In situ* PDF of PMN-0.30PT piezoceramic

In situ PDF analysis is carried out to study the local scale structural response to electric fields in order to better interpret the mechanisms underpinning the properties of PMN-0.30PT piezoceramic. The *in situ* PDF technique, first reported by Usher *et al.*,[36] has been applied to various compositions of piezoceramics.[36,56,57] Figure 6 shows the *in situ* PDF patterns of PMN-0.30PT from 0 kV/mm to 4.0 kV/mm. The directional PDF patterns were obtained from $S(Q)$ in which the scattering vector is approximately *parallel* to the electric field. The three subplots represent different PDF regions of interest. Peak shifts to higher-*r* values at intermediate length scale, as indicated in Fig. 6b and c, due to the field-induced piezoelectric strain. The most interesting observations exist at the local scale, as shown in Fig. 6a: no notable changes under fields (even at the maximum 4.0 kV/mm) for the Pb-Pb peaks at $r\approx4.0$ Å and $r\approx5.8$ Å, and a clear peak splitting for the nearest Pb-B pair at $r\approx3.5$ Å.

The behavior of the PDF peak at $r\approx3.5$ Å can be interpreted in terms of the Pb^{2+} displacements, which are commonly observed in Pb-based perovskites and are expected to be significantly larger than those of B-sites ions. Even though the changes of polarization cannot be fully described since X-ray PDF is not sensitive to the oxygen positions, the Pb^{2+} displacement can still be used to interpret the local structural changes under fields. Figure S11a shows a schematic of Pb^{2+} and its B-site neighbors in the R structure with Pb^{2+} displaced along ⟨111⟩, while Figure S11b illustrates a distribution of Pb-B distances in the T structure with Pb^{2+}

displaced along ⟨001⟩. In perovskites, there are 8 Pb-B pairs denoted as R1-R8. Pb^{2+} displacement along different directions will result in different distributions of Pb-B distances.[13] Not all the Pb-B pairs can be resolved in PDF due to thermal vibrations and the intrinsic disorder of PMN-*x*PT. Therefore, the distribution of the Pb-B distances for R and R-like structures, e.g. M_A with polarization vector near ⟨111⟩, is approximated by 1 short (R_{short}), 6 intermediate (R_{medium}), and 1 long (R_{long}) distances (denoted as the "3-peaks" fitting model); while for T and T-like structures, e.g. M_C with polarization vector toward ⟨001⟩, the distribution is approximated by 4 short (R_{short}) and 4 long (R_{long}) distances (described as the "2-peaks" model hereafter).

These two models are constructed and used to fit the local PDF peaks at r≈3.5 Å at various fields. Representative plots are shown in Fig. 7. For the unpoled sample (Fig. 7a), the r≈3.5 Å peak can be described well with the "3-peaks" model: values for R_{short} of 3.30 Å in red, R_{medium} of 3.57 Å in blue, and R_{long} of 3.88 Å in green. With increasing field, (e.g. up to 1.8 kV/mm), the resolved peak positions remain nearly unchanged, while the R_{medium} peak becomes slightly broader (FWHM changed from 0.28 ± 0.02 Å to 0.36 ± 0.03 Å). For PDFs above 1.8 kV/mm, the local PDF peaks can all fit well with "2-peaks" instead of the "3-peaks" model, indicating the existence of a T or T-like phase. We notice the transition field of local structure (1.8 kV/mm) is slightly larger than the one of long-range structure (1.6 kV/mm), which might because the enhanced distortions of the local structure require higher electric field for transformation.

Even though the PDF analysis is not sensitive enough to differentiate subtle M_A details from R, nor M_C from T, the changes in the distribution of Pb-B distances with increasing field are consistent with a transition from an R-like to a T-like phase, which agrees with the inferences

from our *in situ* XRD study. No qualitative differences in the behaviors of the average and local structure is observed as far as the Pb-Pb and Pb-B distance distributions are concerned.

3.5 Long-range and local scale crystal structure of poled PMN-0.30PT piezoceramic

The *ex situ* XRD and PDF patterns of poled (at 4.0 kV/mm) PMN-0.30PT piezoceramic were obtained. The comparisons of selected Bragg and local PDF peaks, obtained from the poled sample and that under 4.0 kV/mm are illustrated in Fig. S12. For the XRD, when the applied field is removed, the characteristic peak asymmetry and splitting become strongly reduced, and the profile reverts to be similar to the unpoled or low field patterns. Le Bail fitting proves that a monoclinic *Cm* phase gives the best overall fit of the poled PMN-0.30PT. The reversibility of field-induced long-range structure agrees with Noheda *et al.* [58,59] For the PDF, the splitting of the Pb-B pair disappears after the field was removed, which suggests that the local structure reverted back to the M_A or R-like arrangement. The reversibility of the field-induced local-structure changes in PMN-*x*PT gives further confidence that the Pb-B PDF peak behavior is a result of intrinsic changes in the Pb^{2+} displacements rather than of domain reorientation, which is presumed to be irreversible under fields as high as 4.0 kV/mm.[15,60]

4 Conclusions

The electric-field-induced changes in the crystallographic structure of PMN-0.30PT piezoceramic is revealed using *in situ* XRD and PDF. The average and local structure for unpoled PMN-0.30PT piezoceramic near the MPB is monoclinic *Cm*. Under the application of electric fields, polarization rotation and a phase transition from M_A (*Cm*) to M_C (*Pm*) occur. In addition, the *in situ* PDF study also confirms the systematic changes of PMN-0.30PT at the local scale, which provides indications of the intrinsic field-induced polarization rotation. Our study suggests that the reversible field-induced phase transition and polarization rotation are responsible for the origins of high piezoelectric properties at the MPB. It will be interesting to apply the *in situ* techniques to other PMN-*x*PT compositions and other Pb-based relaxor ferroelectrics to study the fundamental mechanisms during the application of electric fields.

Supplemental Materials

See supplemental Materials [URL] for additional XRD fits, PDF refinements, and TEM characterization.

Acknowledgements

This research used resources of the Advanced Photon Source, a U.S. Department of Energy (DOE) Office of Science User Facility operated for the DOE Office of Science by Argonne National Laboratory under Contract No. DE-AC02-06CH11357. The authors acknowledge Kevin Beyer, Olaf Borkiewicz, and Karena Chapman at 11-ID-B for their assistance with the experiments. The authors would like to thank the Slovenian Research Agency for financial support (program P2-0105; projects J2-7526, L2-6768 and PR-06166; bilateral projects: BI-US/15-16-60 and BI-US-17/18-059). D.H. thanks the financial support from China Scholarship Council. T.-M.U., D.H., and J.L.J. acknowledge support from the U.S. Department of Commerce under Award No. 70NANB13H197. This material is based, in part, upon work supported by the National Science Foundation, as part of the Center for Dielectrics and Piezoelectrics under Grant Nos. IIP-1361571 and IIP-1361503. This material is based upon work supported by the U.S. Department of Energy, Office of Science, Office of Basic Energy Sciences under contract number DE-AC05-00OR22725.

1

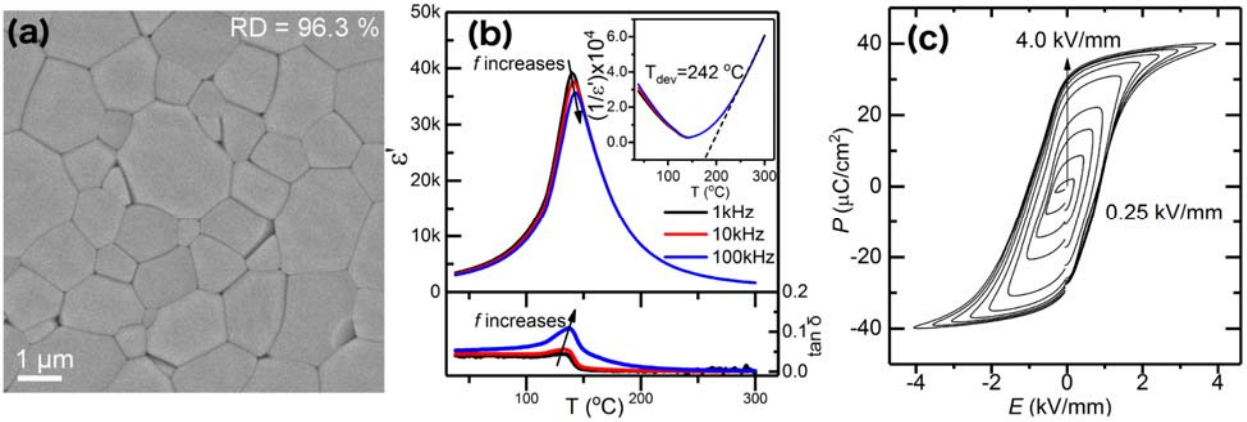

FIG. 1. FE-SEM images (a), dielectric measurements (b), and P-E loops (c) of the PMN-0.30PT piezoceramic. Inset of subplot (b) shows the deviation of Curie-Weiss law; the dashed line shows the linear fit of $(1/\varepsilon')$ versus T at the paraelectric phase.

2

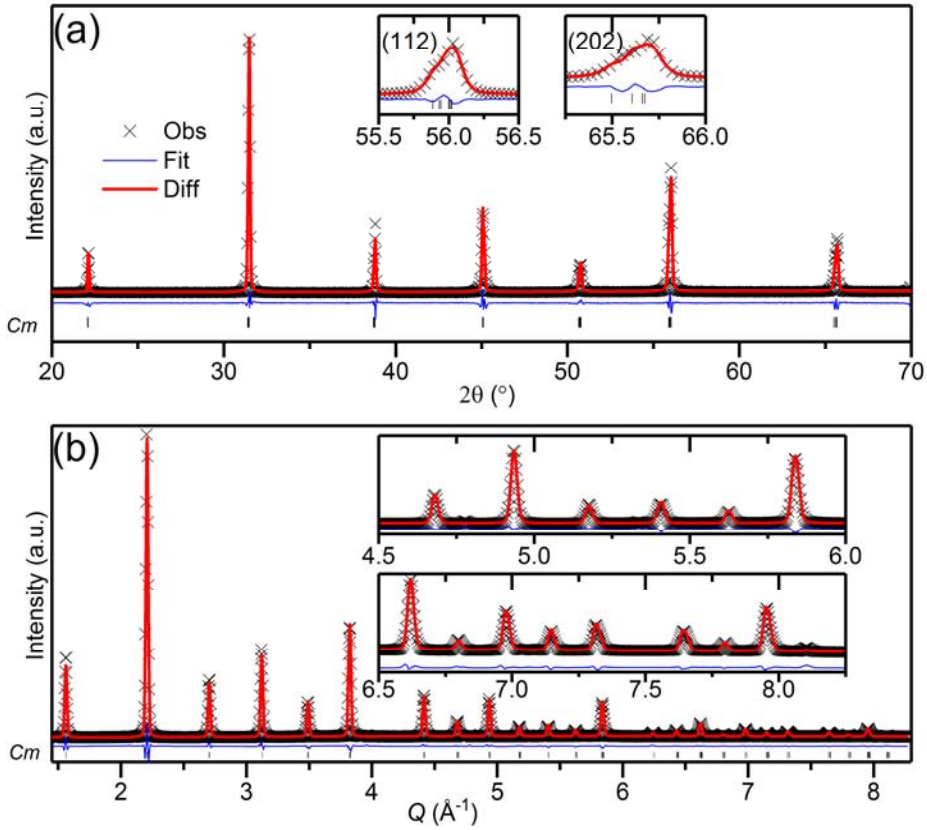

FIG. 2. The overall fit of the unpoled PMN-0.30PT XRD pattern using monoclinic *Cm* structure for laboratory XRD (a) and SXRD (b). The observed XRD is shown as black crosses, the calculated fit in red, and the difference in blue.

1

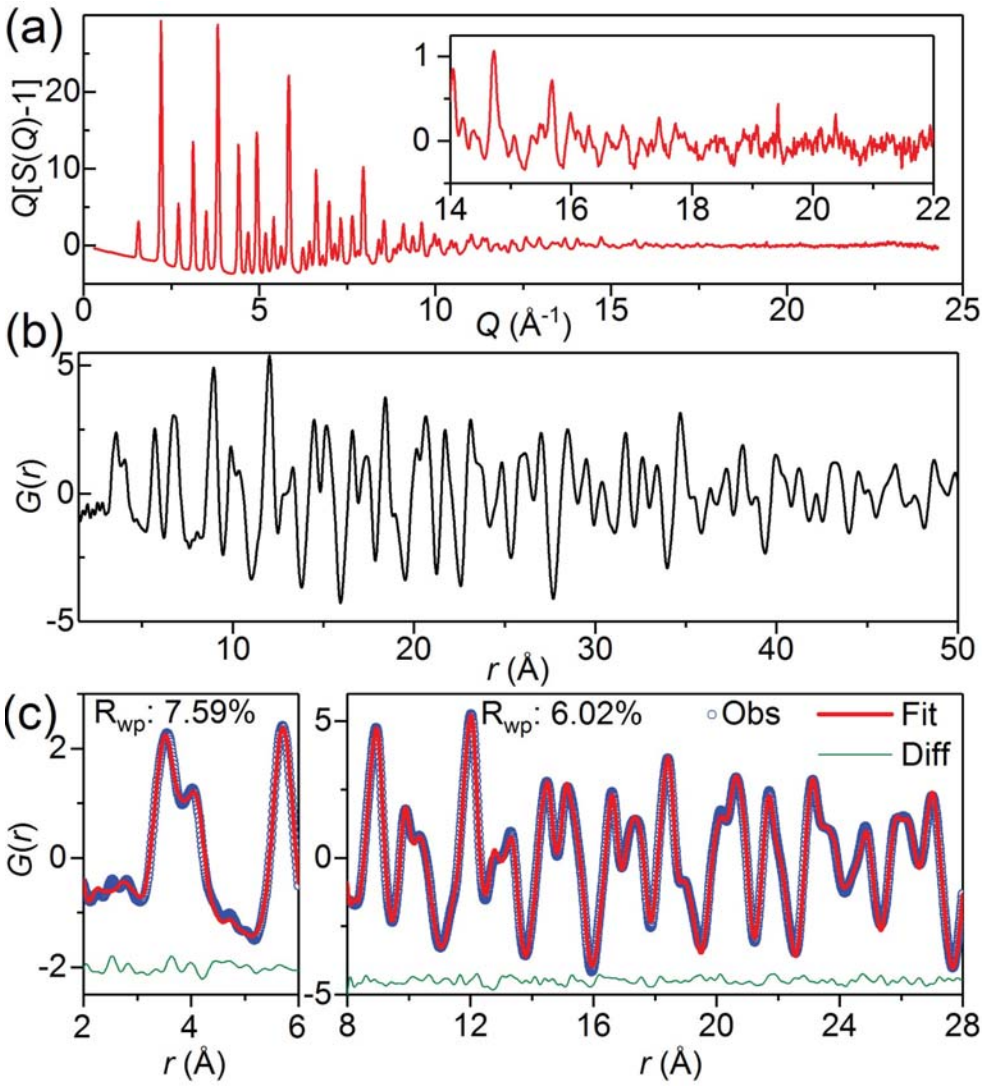

FIG.3. Reduced total scattering function (a), and PDF pattern after Fourier transform (b) of the unpoled PMN-0.30PT piezoceramic. (c) Fits of the unpoled PMN-0.30PT PDF pattern using *Cm* model over a range of 2-6 Å (representing the local scale structure), and over 8-28 Å (representing intermediate scale structure). The observed data is shown as blue circles, the calculated fit in magenta, and the difference in green.

1

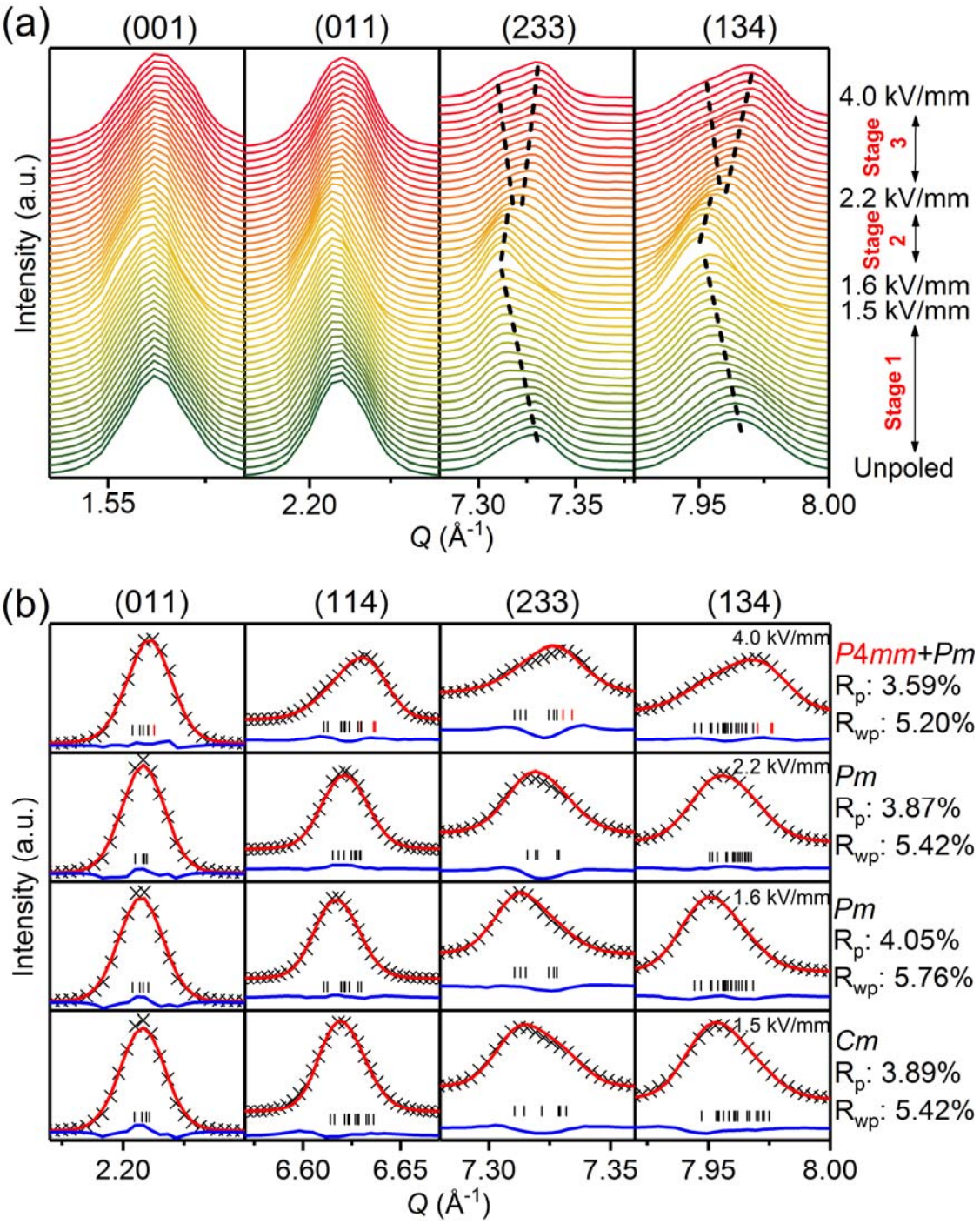

FIG. 4 (a): *In situ* electric field XRD in selected representative *Q* ranges. The process is categorized into 3 stages. (b): the best fits using specific model for patterns at 1.5 kV/mm, 1.6 kV/mm, 2.2 kV/mm, and 4.0 kV/mm, respectively. Note for 4.0 kV/mm pattern a *P*4*mm*(red)+*Pm*(black) mixed phase model was adopted.

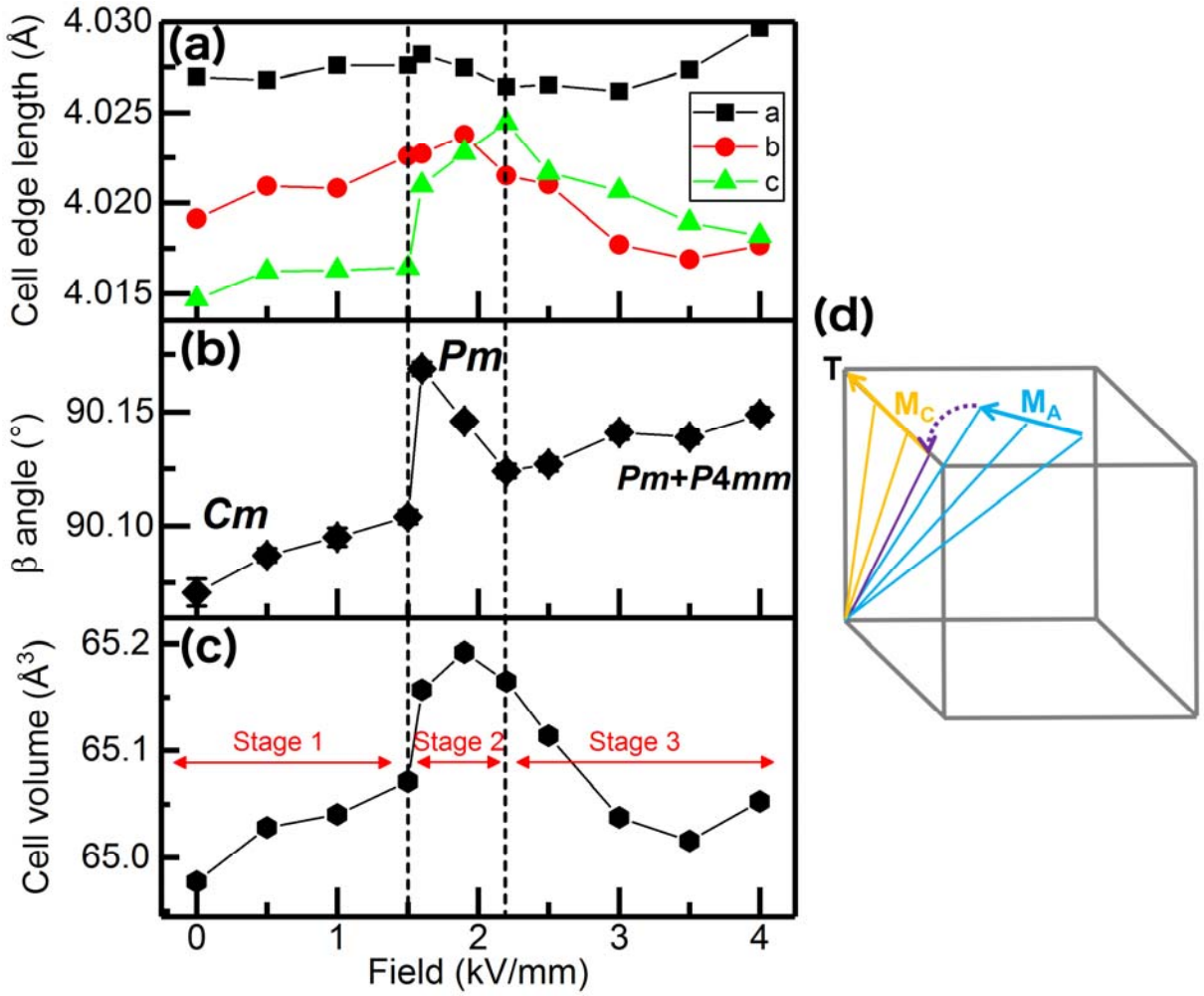

FIG. 5. Lattice parameters: cell edge length (a), β angle (b), and cell volume (c) of PMN-0.30PT under various fields obtained from the Le Bail fitting. The assigned stage numbers and identified structures are noted. (d) Polarization rotation path for PMN-0.30PT piezoceramic proposed by this study. For the patterns fitted with mixed-phase model, only structure information of *Pm* is plotted.

1

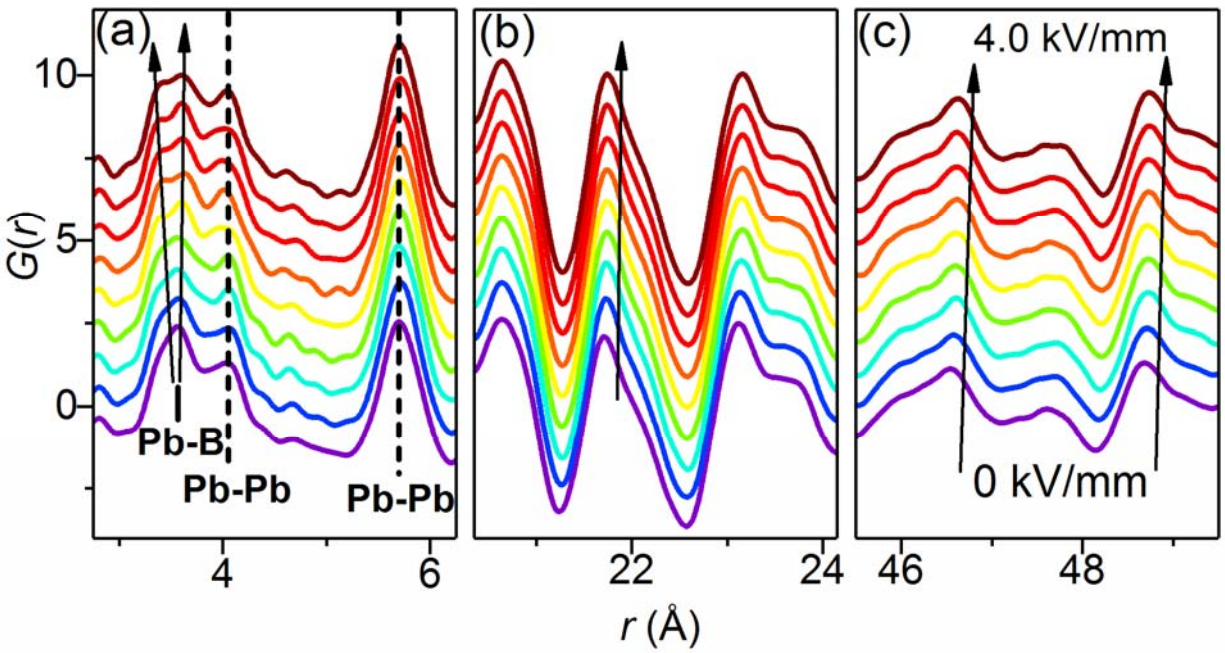

FIG. 6. *In situ* electric field PDF patterns from 0 kV/mm to 4.0 kV/mm at different length scales. The arrows indicate the evolution of PDF peaks with increasing fields. The dashed lines in subplot (a) show the negligible changes of nearest and second nearest Pb-Pb pairs with increasing field.

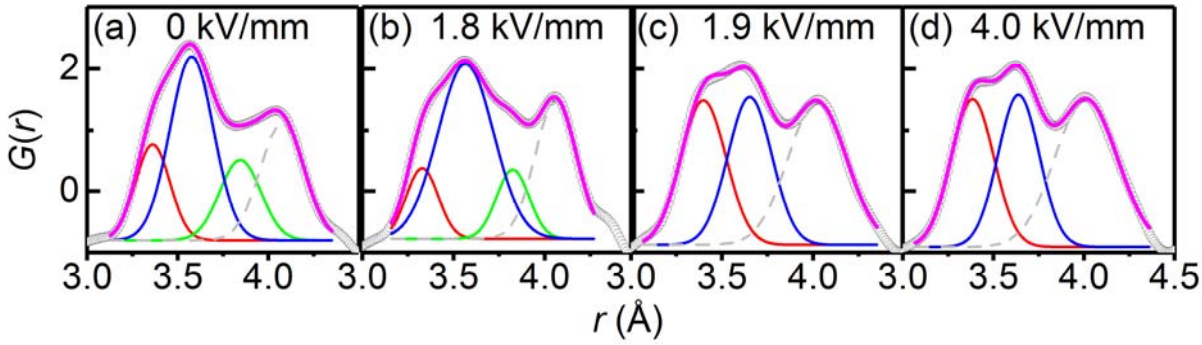

FIG. 7. Representative fits of Pb-B local PDF peaks at r≈3.5 Å under selected fields. The observed data is shown as blue circles, the sum fit in magenta, and the resolved individual peaks in red, blue, or green. Subplot (a) and (b) shows "3-peaks" model fits well for 0-1.8 kV/mm patterns. Subplot (c) and (d) show "2-peaks" model better represents the high-field local structures. The grey dash line shows the fits of local Pb-Pb PDF peaks at r≈4.0 Å.

References

[1] G. Burns and F.H. Dacol, Phys. Rev. B **28**, 2527 (1983).
[2] D. Fu, H. Taniguchi, M. Itoh, S.Y. Koshihara, N. Yamamoto, and S. Mori, Phys. Rev. Lett. **103**, 2 (2009).
[3] A.A. Bokov, B.J. Rodriguez, X. Zhao, J.-H. Ko, S. Jesse, X. Long, W. Qu, T.H. Kim, J.D. Budai, A.N. Morozovska, and S. Kojima, Zeitschrift Für Krist. **226**, 99 (2011).
[4] Z.-G. Ye, Y. Bing, J. Gao, A.A. Bokov, P. Stephens, B. Noheda, and G. Shirane, Phys. Rev. B **67**, 104104 (2003).
[5] Z.-G. Ye, MRS Bull. **34**, 277 (2009).
[6] A.A. Bokov and Z.-G. Ye, J. Mater. Sci. **41**, 31 (2006).
[7] S.-E. Park and T.R. Shrout, J. Appl. Phys. **82**, 1804 (1997).
[8] D. Phelan, E.E. Rodriguez, J. Gao, Y. Bing, Z.-G. Ye, Q. Huang, J. Wen, G. Xu, C. Stock, M. Matsuura, and P.M. Gehring, Phase Transitions **88**, 283 (2015).
[9] A.K. Singh, D. Pandey, and O. Zaharko, Phys. Rev. B **74**, 24101 (2006).
[10] B. Noheda, D.E. Cox, G. Shirane, J. Gao, and Z.-G. Ye, Phys. Rev. B **66**, 54104 (2002).
[11] R.A. Cowley, S.N. Gvasaliya, S.G. Lushnikov, B. Roessli, and G.M. Rotaru, Adv. Phys. **60**, 229 (2011).
[12] S. Zhang and F. Li, J. Appl. Phys. **111**, 1 (2012).
[13] T. Egami, Annu. Rev. Mater. Res. **37**, 297 (2007).
[14] A.A. Bokov and Z.-G. Ye, J. Adv. Dielectr. **2**, 1241010 (2012).
[15] D. Damjanovic, Reports Prog. Phys. **61**, 1267 (1998).
[16] L.E. Cross, Ferroelectrics **76**, 241 (1987).
[17] H. Fu and R.E. Cohen, Nature **403**, 281 (2000).
[18] B. Noheda, Curr. Opin. Solid State Mater. Sci. **6**, 27 (2002).
[19] Z. Kutnjak, J. Petzelt, and R. Blinc, Nature **441**, 956 (2006).
[20] Y.M. Jin, Y.U. Wang, A.G. Khachaturyan, J.F. Li, and D. Viehland, Phys. Rev. Lett. **91**, 197601 (2003).
[21] F. Li, S. Zhang, T. Yang, Z. Xu, N. Zhang, G. Liu, J. Wang, J. Wang, Z. Cheng, Z.-G. Ye, J. Luo, T.R. Shrout, and L.-Q. Chen, Nat. Commun. **7**, 13807 (2016).
[22] M. Davis, J. Electroceramics **19**, 25 (2007).
[23] M. Algueró, C. Alemany, B. Jiménez, J. Holc, M. Kosec, and L. Pardo, J. Eur. Ceram. Soc. **24**, 937 (2004).
[24] H. Uršič, L. Fulanović, M. Vrabelj, Z. Kutnjak, B. Rožič, S. Drnovšek, and B. Malič, Adv. Appl. Ceram. **115**, 77 (2016).
[25] M. Vrabelj, H. Uršič, Z. Kutnjak, B. Rožič, S. Drnovšek, A. Benčan, V. Bobnar, L. Fulanović, and B. Malič, J. Eur. Ceram. Soc. **36**, 75 (2016).
[26] D. Damjanovic, Appl. Phys. Lett. **97**, 62906 (2010).
[27] T. Iamsasri, G. Tutuncu, C. Uthaisar, S. Wongsaenmai, S. Pojprapai, and J.L. Jones, J. Appl. Phys. **117**, 24101 (2015).
[28] E. Aksel, J.S. Forrester, J.L. Jones, P.A. Thomas, K. Page, and M.R. Suchomel, Appl. Phys. Lett. **98**, 152901 (2011).
[29] M.B. Smith, K. Page, T. Siegrist, P.L. Redmond, E.C. Walter, R. Seshadri, L.E. Brus, and M.L. Steigerwald, J. Am. Chem. Soc. **130**, 6955 (2008).
[30] H. Liu, J. Chen, L. Fan, Y. Ren, L. Hu, F. Guo, J. Deng, and X. Xing, Chem. Mater. **29**, 5767 (2017).

[31] H. Liu, J. Chen, L. Fan, Y. Ren, Z. Pan, K. V. Lalitha, J. Rödel, and X. Xing, Phys. Rev. Lett. **119**, 17601 (2017).
[32] G. Esteves, C.M. Fancher, and J.L. Jones, J. Mater. Res. **30**, 340 (2015).
[33] J.L. Jones, J. Electroceramics **19**, 69 (2007).
[34] P.J. Chupas, X. Qiu, J.C. Hanson, P.L. Lee, C.P. Grey, and S.J.L. Billinge, J. Appl. Crystallogr. **36**, 1342 (2003).
[35] P.J. Chupas, K.W. Chapman, and P.L. Lee, J. Appl. Crystallogr. **40**, 463 (2007).
[36] T.-M. Usher, I. Levin, J.E. Daniels, and J.L. Jones, Sci. Rep. **5**, 14678 (2015).
[37] A. Hammersley, Eur. Synchrotron Radiat. Facil. Intern. Rep. ESRF97HA02T 1 (1997).
[38] A.C. Larson and R.B. Von Dreele, Los Alamos Natl. Lab. Rep. LAUR 86 (2000).
[39] B.H. Toby, J. Appl. Crystallogr. **34**, 210 (2001).
[40] P. Juhás, T. Davis, C.L. Farrow, and S.J.L. Billinge, J. Appl. Crystallogr. **46**, 560 (2013).
[41] C.L. Farrow, P. Juhas, J.W. Liu, D. Bryndin, E.S. Božin, J. Bloch, T. Proffen, and S.J.L. Billinge, J. Phys. Condens. Matter **19**, 335219 (2007).
[42] O. Noblanc, P. Gaucher, and G. Calvarin, J. Appl. Phys. **79**, 4291 (1996).
[43] A.K. Singh and D. Pandey, Phys. Rev. B **67**, 64102 (2003).
[44] Z.-G. Ye, B. Noheda, M. Dong, D. Cox, and G. Shirane, Phys. Rev. B **64**, 184114 (2001).
[45] D. Vanderbilt and M.H. Cohen, Phys. Rev. B **63**, 94108 (2001).
[46] N. Zhang, H. Yokota, A.M. Glazer, Z. Ren, D.A. Keen, D.S. Keeble, P.A. Thomas, and Z.-G. Ye, Nat. Commun. **5**, 5231 (2014).
[47] I.-K. Jeong, T.W. Darling, J.K. Lee, T. Proffen, R.H. Heffner, J.S. Park, K.S. Hong, W. Dmowski, and T. Egami, Phys. Rev. Lett. **94**, 147602 (2005).
[48] W. Dmowski, M.K. Akbas, P.K. Davies, and T. Egami, J. Phys. Chem. Solids **61**, 229 (2000).
[49] A. Le Bail, Powder Diffr. **20**, 316 (2005).
[50] M. Ahart, M. Somayazulu, R.E. Cohen, P. Ganesh, P. Dera, H. Mao, R.J. Hemley, Y. Ren, P. Liermann, and Z. Wu, Nature **451**, 545 (2008).
[51] Z. Chen, S. Prosandeev, Z.L. Luo, W. Ren, Y. Qi, C.W. Huang, L. You, C. Gao, I.A. Kornev, T. Wu, J. Wang, P. Yang, T. Sritharan, L. Bellaiche, and L. Chen, Phys. Rev. B - Condens. Matter Mater. Phys. **84**, 1 (2011).
[52] M. Davis, D. Damjanovic, and N. Setter, Phys. Rev. B **73**, 14115 (2006).
[53] P. Finkel, M. Staruch, A. Amin, M. Ahart, and S.E. Lofland, Sci. Rep. **5**, 13770 (2015).
[54] Y.H. Bing, A.A. Bokov, and Z.-G. Ye, Curr. Appl. Phys. **11**, 14 (2011).
[55] F. Bai, N. Wang, J. Li, D. Viehland, P.M. Gehring, G. Xu, and G. Shirane, J. Appl. Phys. **96**, 1620 (2004).
[56] A.J. Goetzee-Barral, T.-M. Usher, T.J. Stevenson, J.L. Jones, I. Levin, A.P. Brown, and A.J. Bell, Phys. Rev. B **96**, 14118 (2017).
[57] I. Levin, V. Krayzman, J.C. Woicik, F. Bridges, G.E. Sterbinsky, T.-M. Usher, J.L. Jones, and D. Torrejon, Phys. Rev. B **93**, 104106 (2016).
[58] B. Noheda, Z. Zhong, D.E. Cox, G. Shirane, S.-E. Park, and P. Rehrig, Phys. Rev. B **65**, 224101 (2002).
[59] B. Noheda, D.E. Cox, G. Shirane, S.-E. Park, L.E. Cross, and Z. Zhong, Phys. Rev. Lett. **86**, 3891 (2001).
[60] D. Bolten, U. Böttger, and R. Waser, J. Appl. Phys. **93**, 1735 (2003).

Appendix

List of figures in the paper:

FIG. 1. FE-SEM images (a), dielectric measurements (b), and P-E loops (c) of the PMN-0.30PT piezoceramic. Inset of subplot (b) shows the deviation of Curie-Weiss law; the dashed line shows the linear fit of (1/ε') versus T at the paraelectric phase.

FIG. 2. The overall fit of the unpoled PMN-0.30PT XRD pattern using monoclinic *Cm* structure for laboratory XRD (a) and SXRD (b). The observed XRD is shown as black crosses, the calculated fit in red, and the difference in blue.

FIG. 3. Reduced total scattering function (a), and PDF pattern after Fourier transform (b) of the unpoled PMN-0.30PT piezoceramic. (c) Fits of the unpoled PMN-0.30PT PDF pattern using *Cm* model over a range of 2-6 Å (representing the local scale structure), and over 8-28 Å (representing intermediate scale structure). The observed data is shown as blue circles, the calculated fit in magenta, and the difference in green.

FIG. 4 (a): In situ electric field XRD in selected representative Q ranges. The process is categorized into 3 stages. (b): the best fits using specific model for patterns at 1.5 kV/mm, 1.6 kV/mm, 2.2 kV/mm, and 4.0 kV/mm, respectively. Note for 4.0 kV/mm pattern a P4mm(red)+Pm(black) mixed phase model was adopted.

FIG. 5. Lattice parameters: cell edge length (a), β angle (b), and cell volume (c) of PMN-0.30PT under various fields obtained from the Le Bail fitting. The assigned stage numbers and identified structures are noted. (d) Polarization rotation path for PMN-0.30PT pizeoceramic proposed by this study. For the patterns fitted with mixed-phase model, only structure information of Pm is plotted.

FIG. 6. In situ electric field PDF patterns from 0 kV/mm to 4.0 kV/mm at different length scales. The arrows indicate the evolution of PDF peaks with increasing fields. The dashed lines in subplot (a) show the negligible changes of nearest and second nearest Pb-Pb pairs with increasing field.

FIG. 7. Representative fits of Pb-B local PDF peaks at r≈3.5 Å under selected fields. The observed data is shown as blue circles, the sum fit in magenta, and the resolved individual peaks in red, blue, or green. Subplot (a) and (b) shows "3-peaks" model fits well for 0-1.8 kV/mm patterns. Subplot (c) and (d) show "2-peaks" model better represents the high-field local structures. The grey dash line shows the fits of local Pb-Pb PDF peaks at r≈4.0 Å.

List of figures in the supplementary material:

Figure S1 The degree of asymmetry for the selected peaks, calculated by (AL-AR)/(AL+AR), where AL is the peak area of left side half peak, and AR is the area of right side half peak.

Figure S2 Magnified views of representative Bragg peaks of the high-energy XRD pattern of unpoled PMN-0.30PT, and the fits using different single phase models. The observed XRD is shown as black crosses, the calculated fit in red, and the difference in blue. The hkl indices of these reflections are labeled in a pseudocubic unit cell.

Figure S3 (a) The patterns from different azimuthal sectors (χ) of 2D SXRD image of the pristine sample. The dot lines in (b) and (c) are the difference curves of different azimuthal sectors with $\chi(0°)$ for (112) and (202) peaks, respectively. The majority of the differences curves are smaller than the errors of counting statistics (shown as grey error bars), indicating the patterns are essentially equivalent.

Figure S4 (a) Dark-field TEM image recorded with g=002 reflections reveals twin domains of 10-25 nm thick. (b) SAED confirms extensive structured diffuse scattering due to correlated displacements.

Figure S5 The local PDF peaks for the unpoled (black solid line) and the calculated pattern from a cubic Pm3m prototypic model (black dot line). The asymmetric feature of the r≈3.5 Å Pb-B pair peak and the deviation of peak height from the model are evidenced.

Figure S6 Fits of the unpoled PMN-0.30PT PDF pattern using different single phase models over a range of 2-6 Å (representing the local scale structure), and over 8-28 Å (representing intermediate scale structure). The observed data is shown as blue circles, the calculated fit in red, and the difference in green.

Figure S7 (a) The magnified plots of representative Bragg peaks of the high-energy XRD pattern at 1.5 kV/mm, and the fits using different single phase models. (b) The overall fit of the full pattern using monoclinic Cm structure. The observed XRD is shown as black crosses, the calculated fit in red, and the difference in blue.

Figure S8 (a) The magnified plots of representative Bragg peaks of the high-energy XRD pattern at 1.6 kV/mm, and the fits using different single phase models. Note even though Amm2 gives lower R-values than Pm, by examining the actual fit, the Pm fits the individual reflections better (b) The overall fit of the full pattern using monoclinic Pm structure. The observed XRD is shown as black crosses, the calculated fit in red, and the difference in blue.

Figure S9 (a) The magnified plots of representative Bragg peaks of the high-energy XRD pattern at 2.2 kV/mm, and the fits using different single phase models. (b) The overall fit of the full pattern using monoclinic Pm structure. The observed XRD is shown as black crosses, the calculated fit in red, and the difference in blue.

Figure S10 (a) The magnified plots of representative Bragg peaks of the high-energy XRD pattern at 4.0 kV/mm, and the fits using different single phase models. (b) The overall fit of the

full pattern using Pm+P4mm structure. The observed XRD is shown as black crosses, the calculated fit in red, and the difference in blue.

Figure S11 The schematic of R (a) and T (b) unit cells with the eight individual Pb-B pairs. The Pb^{2+} (centered in green) is coordinated by 8 B-site ions (in black). For R ⟨111⟩, the 8 Pb-B pairs are approximated by 1 short (red), 6 intermediate (blue), and 1 long (green). For T ⟨001⟩, the 8 Pb-B pairs are approximated by 4 short (red) and 4 long (blue).

Figure S12 (a) Selected Bragg peaks of 4.0 kV/mm (in red) and poled PMN-0.30PT (in green). (b) Local PDF peaks of 4.0 kV/mm and poled PMN-0.30PT piezoceramics.

List of tables in the supplementary material:

Table S1 Refined lattice parameters and Bragg fitting values for the SXRD and laboratory XRD using a monoclinic *Cm* structure. By checking the actual fit, the larger R_{wp} and R_p of laboratory XRD refinement might majorly attribute to the better dataset resolution.

Table S2 Refined atomic positions and U_{iso} for the for the SXRD and laboratory XRD using a monoclinic *Cm* structure.